A Comparison between Two Cell Designs for Electrochemical Neodymium Reduction Using Numerical Simulation

TIM HAAS, SIMON HILGENDORF, HANNO VOGEL, BERND FRIEDRICH, and HERBERT PFEIFER

Nowadays, neodymium is almost solely produced by the electrochemical reduction of Neodymium oxide in fused fluoride salts. Thereby, the fluid flow distribution within the electrolysis cell is important for the productivity and efficiency of the process. In this work, the flow field within a conventional cell with vertical electrodes is compared to that of an innovative cell concept with horizontal electrodes by computational fluid dynamics. The numerical model uses the Eulerian volume of fluid approach to track phase boundaries between the continuous phases, while the Lagrangian discrete phase model is applied to compute the rising trajectories of emitted off-gas bubbles. The calculated results indicate that the new cell type is more suitable for the efficient, large-scale production of neodymium, since there is potential to decrease the cell voltage and enhance the current efficiency. By that, the specific energy consumption can be lowered significantly. However, an advanced level of automation is necessary to operate the new cell.

DOI: 10.1007/s11663-017-0982-0

I. INTRODUCTION

THE rare-earth metal neodymium is a key component of strong permanent magnets, which are essential for the production of modern electronics and wind energy devices. In 2002, approximately 95 pct[1] of the worldwide neodymium supply was provided by China. There, more than 95 pct[2] of the neodymium metal is reduced electrochemically by the electrolysis of Neodymium oxide dissolved in fused fluoride salts. This can be explained by the great advantages the process has over alternative methods such as metallothermal reduction or electrochemical reduction in fused chlorides.[1,2] In industrial processes, the electrolyte consists of 10 to 20 wt pct LiF and 80 to 90 wt pct NdF_3 and the process temperature is about 1323 K (1050 °C).[2,3] Depending on process parameters, especially the anode current density and the temperature, carbon monoxide or carbon dioxide is formed at the anode and provides stirring within the cell. According to Faraday's law, the productivity of the electrolysis cell is directly proportional to its current. It needs to be considered, though, that increasing the total cell current also raises the current density at both electrodes. By this, the ion transport through the thin diffusion layer may become the reaction rate determining phenomenon, which would cause the emission of environmental hazardous carbon fluorides at the anode[4] and the electrochemical reduction of product impurities at the cathode. The emission problem is particularly critical, because the solubility of Neodymium oxide in the electrolyte is merely about 2 to 4 wt pct.[5]

Facing this problem, efficient mixing is important to homogenize the electrolyte and enhance the dissolution of added oxide. However, the mixing must not be too violent, as reduced neodymium droplets might be transported to the anode and reoxidize. This causes a loss in current efficiency. The problem might be overcome by a broader distance between the electrodes. However, this results in a high specific energy as the cell voltage increases. In order to have a productive and efficient cell without the drawbacks mentioned previously, detailed knowledge of the fluid flow distribution is crucial.

To this day, the standard 3-kA cell consists of a vertically inserted, perpendicular tungsten rod connected as the cathode, which is surrounded by a graphite hollow cylinder used as the anode. Owing to the highly corrosive electrolyte, the crucible is made of graphite as

TIM HAAS and HERBERT PFEIFER are with the Department of Industrial Furnaces and Heat Engineering, RWTH Aachen University, Kopernikusstraße 10, 52074 Aachen, Germany. Contact e-mail: haas@iob.rwth-aachen.de SIMON HILGENDORF, HANNO VOGEL, and BERND FRIEDRICH are with IME Process Metallurgy and Metal Recycling, RWTH Aachen University, Intzestrasse 3, 52062 Germany.

Manuscript submitted July 5, 2016.
Article published online May 8, 2017.

well. The reduced metal is liquidly collected in a tungsten crucible placed beneath the cathode.[6] Since the tungsten crucible is easy to reach, the product withdrawal is simple. Usually, this is performed with a titanium ladle. Although this standard cell type is easy to handle and is well known by the operators, it has significant disadvantages. For instance, a high specific energy of about 9.5 to 11 kWh/kg,[2] respectively, 11 to 13 kWh/kg,[6] caused by a broad electrode distance; a large free surface area resulting in a significant heat loss; and a relative low current efficiency caused by product reoxidation.

In order to overcome these drawbacks, a new cell type, similar to the Hall–Héroult cell known from aluminum reduction, was designed. This cell consists of a graphite anode and a horizontal cathode formed by an already reduced molten metal pool.[2] In this cell, the electrode distance and the free surface area can be decreased significantly. First experiments in laboratory scale cells revealed that the cell voltage could be decreased from 10 to 15 V to 5 to 6 V.[7] Moreover, larger electrodes can be easily installed without changing the sedimentation path of reduced neodymium metal. This opportunity is crucial to fulfill the growing demand for neodymium.

Owing to the corrosiveness and high temperature of the electrolyte, online physical measurements in running reduction cells are nearly impossible. Because of that, cell design improvement should be assisted by CFD simulations. First computational studies, for the old cell type as well as for the new cell type, were conducted in China. Wang *et al.*[8] simulated the impact of the electrode distance to the fluid flow within a 10-kA bottom cathode cell. Ren *et al.*[9] investigated the fluid flow in a 3-kA cell with the conventional cell design but with the anode instead of the cathode in the center. He *et al.*[10] calculated the fluid field in a 3-kA cell as well but took both electromagnetic force and gas bubbles into account. Nevertheless, there are no studies published so far in which the fluid flows in both cells are compared directly.

Thus, the objective of this work is to calculate and compare the fluid flow field in both the conventional and the modern cell design and to discuss the effect of the fluid flow on the crucial process parameters introduced previously.

II. MODEL DESCRIPTION

The electrolysis process is characterized by a high complexity in regard to numerical modeling. The fluid flow is the result of three different phenomena: natural convection caused by temperature- or concentration-related density gradients, an electromagnetic stirring force, and fluid motion induced by rising anode gas bubbles. In the present work, only the gas stirring is taken into account, as the cell's total current is relatively low and the temperature and concentration distribution are assumed to be homogenous. Owing to that, the anode gas stirring impact on the fluid flow exceeds those of natural convection and electromagnetic forces by far. Despite these simplifications, four different phases, respectively, three phases in case of the conventional cell design, still need to be taken into account. In the modern cell design, a continuous liquid neodymium metal phase exists at the cell's bottom, which forms the cathode. Above that, a continuous fused salt electrolyte phase is located. In addition, a continuous air phase is taken into account in order to model the free electrolyte surface above the electrolyte. The phase distribution within both cells is depicted in Figure 1. The fourth, respectively, third, phase is the anode gas, which is dispersed in small bubbles. The interfaces between the three continuous phases (metal, electrolyte, and air) are tracked by the Eulerian volume of fluid model by Hirt and Nichols.[11] For the anode gas, the Lagrangian discrete phase model is used. In the Lagrangian approach, the bubble trajectories are modeled independent of the mesh by balancing all impacting forces. Owing to that, bubbles smaller than the mesh size can be modeled and the mesh requirements are lower. Since the forces that are taken into account for the force balance are crucial for the accuracy of the numerical model, they are discussed in detail subsequently. The description of variables used in the thereby used equations are listed in Table I.

The cell's dimensions and phase distribution are in accordance with currently operated cells mentioned in publications.[8] However, in order to make the results comparable, the anode injection depth for the conventional cell is slightly modified so that both cells have the same anodic current density. The cell's dimensions are given in Figure 1. For the calculation of the modern cell, a structured mesh that contains 1,154,430 hexahedral cells is applied on the geometry. To improve the quality of the mesh, it contains an O-grid located around the symmetry axis. On all surfaces, a no-slip boundary condition is applied, except for the wall above the air, at which a zero-shear condition is used. The zero-shear condition proved to support the numerical stability of the phase boundary computation. For the conventional cell, the computation is conducted on 1,212,276 hexahedral cells comprising mesh, on which the same boundary conditions are applied.

Small current densities on the anode sidewalls, which do not face the cathode directly, are neglected, so the entire anode gas is emitted at the anode side facing the cathode. The amount of emitted anode gas is calculated by Faraday's law, assuming that the anode gas consists merely of carbon monoxide. This is in accordance with experimental studies by Liu *et al.*[13] and Vogel *et al.*[4] With a current of 10 kA for the new cell and 3 kA for the conventional cell, the calculated gas rate is 1.824 g/s, respectively, 0.548 g/s. The physical properties used are listed in Table II. The electrolyte composition as well as the electrolyte temperature is assumed to be homogenous.

All anode gas bubbles are assumed to have a diameter of 4 mm. The bubble diameter assumption is based on experimental results by Alam *et al.*[14] in a water model of the aluminum Hall–Héroult cell. It should be noticed, though, that the bubble diameter in fused salt electrolysis is difficult to measure and might vary significantly

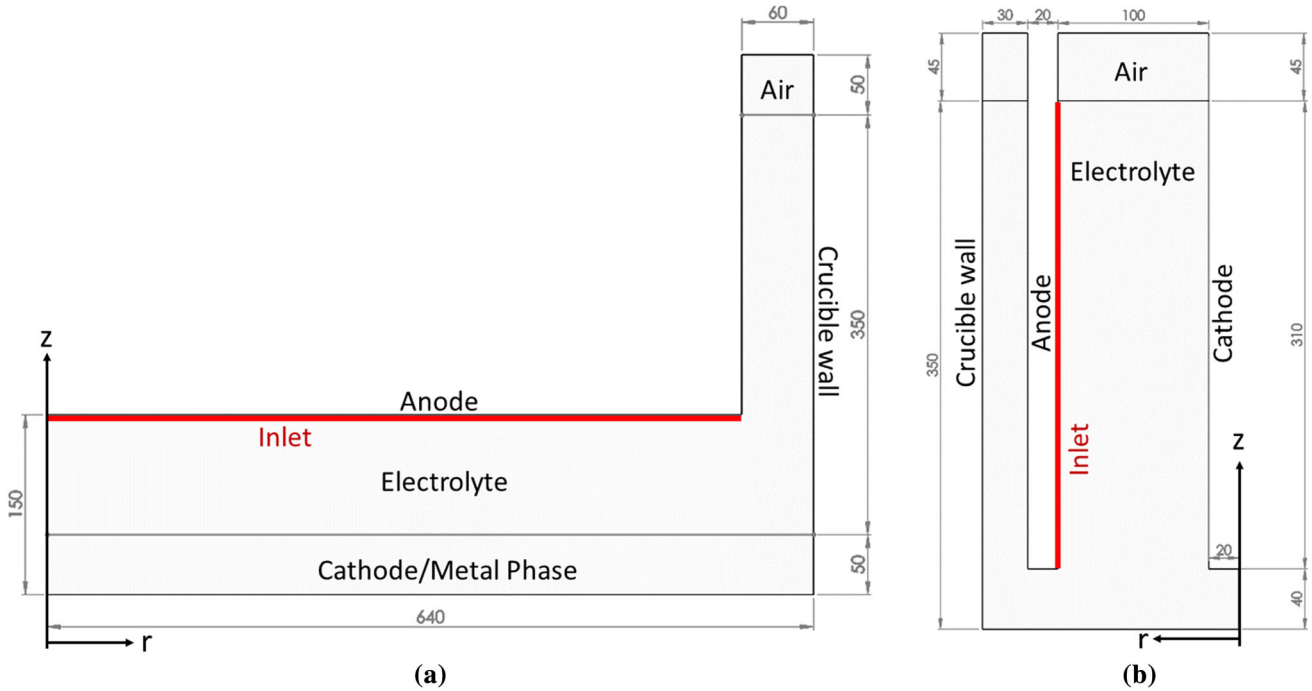

Fig. 1—Geometric model and phase distribution of the (*a*) modern and (*b*) conventional cell with equivalent anodic current density (lengths in millimeters).

Table I. List of Symbols

Symbol	Description
a	gas bubble major semiaxis (m)
Ca	capillary number
C_D	drag coefficient
d_B	gas bubble diameter (m)
F_B	buoyancy force (N)
F_D	drag force (N)
F_{ex}	bubble force on continuous phase (N)
f	friction factor
Eo	Eötvös number
g	gravitational acceleration (m/s^2)
Mo	Morton number
$\dot{m}_B$	gas bubble mass flow rate (kg/s)
Re_B	gas bubble Reynolds number
R_{eq}	equilibrium bubble diameter (m)
Δt	time-step (s)
u_B	gas bubble velocity (m/s)
u_C	electrolyte velocity (m/s)
V_B	bubble volume (m^3)
ρ_B	density anode gas (kg/m^3)
ρ_C	density electrolyte (kg/m^3)
μ_C	dynamic viscosity electrolyte (Pa s)
σ	surface tension (N/m)

from this value. Moreover, the bubble diameter is not necessarily the same for the different cell types. In the case of the modern cell design, the bubbles are released into the computational domain randomly distributed below the anode surface indicated in Figure 1(a). All bubbles that are in the anode center, more specifically in a radius smaller than 0.54 m around the symmetry axis, are deleted immediately. These bubbles would remain in the computational domain for a long period and, therefore, would decrease the efficiency of the calculation significantly. A more adequate modeling would require the description of the outwardly directed drift motion along the anode surface. Bubbles that reach the anode edge are accelerated toward the free surface by the buoyancy force:

$$F_B = (\rho_C - \rho_B) g V_B \quad [1]$$

Additionally, a drag force acts against the direction of movement. This force comprises, in fact, two phenomena: a viscous friction force and a force caused by a pressure gradient along the bubble surface in the direction of movement. The local pressure gradient is the result of the bubble wake and, therefore, is more pronounced in the case of high bubble Reynolds numbers Re_B:

$$Re_B = \frac{\text{Inertia}}{\text{Viscous drag force}} = \frac{\rho_C \left| \vec{u}_B - \vec{u}_C \right| d_B}{\mu_C} \quad [2]$$

Generally, the drag force is given by

$$F_D = C_D \frac{\pi}{4} d_B^2 \frac{\rho_C}{2} \left(\vec{u}_C - \vec{u}_B \right)^2 \quad [3]$$

Equation 3 indicates that the drag force is directly proportional to the dimensionless drag coefficient C_D, which depends on bubble properties and the flow conditions. Numerous attempts to determine C_D are

Table II. Employed Physical Properties [1323 K (1050 °C), 87 Wt Pct NdF_3, 2 Wt Pct Nd_2O_3]

Property	Unit	Value	References
Electrolyte density	kg/m^3	4060	12
Electrolyte viscosity	Pa s	4.95×10^{-3}	8
Electrolyte surface tension	N/m	0.270	13
Molten metal density	kg/m^3	6720	1
Molten metal viscosity	Pa s	4.95×10^{-3}	(assumed)
Anode gas density	kg/m^3	0.296	8
Anode gas viscosity	Pa s	0.04881×10^{-3}	8
Bubble diameter (uniform)	m	4×10^{-3}	14

available. The correlations are either analytical or empirical in nature. Analytical approximations are only possible in the case of inviscid flows (Re $\rightarrow \infty$) or creeping flows (Re$\rightarrow$0). Owing to that, they are often not applicable reasonably for real flows. Frank *et al.*[15] showed that the correlation that is in best accordance with experimental results is that of Tomiyama *et al.*,[16] which, therefore, is implemented in this work:

$$C_D = \max\left[\min\left[\frac{24}{Re_B}\left(1 + 0.15Re_B^{0.687}\right), \frac{72}{Re_B}\right], \frac{8}{3}\frac{Eo}{Eo+4}\right] \quad [4]$$

Tomiyama *et al.*[16] formulated a different drag correlation for three different degrees of contamination. In this work, the equation for fully contaminated systems is used, since it is assumed that the bubbles interact with solid inclusions such as undissolved oxide powder or solidified electrolyte particles. The correlation takes into account that for larger bubbles, the rising velocity is almost independent of the viscose friction. Therefore, it is no longer described by the bubble Reynolds number but by the Eötvös number:

$$Eo = \frac{\text{Buoyancy force}}{\text{Surface tension}} = \frac{g(\rho_c - \rho_B)d_B^2}{\sigma} \quad [5]$$

Above a critical Reynolds number, gas bubbles do not raise straight but in spiraling or zigzagging motion. This indicates the existence of a net lift force. By wake analysis with dye[17] or digital particle image velocity,[18] it can be shown that this is the result of an unsteady wake, which induces local pressure gradients at the bubble base. The lift force is not considered in the force balance, though. One reason is that the bubble Reynolds number is expected to be close to the critical Reynolds number; the other reason is that most of the lateral motion occurs on a scale below the applied grid scale and, therefore, cannot be resolved.

On their rising path, the bubbles grow slightly because of a declining static pressure. This is implemented in the model according to

$$d_B(z) = d_{B,0}\left(\frac{\rho_C g H + p_0}{\rho_C g(H - z) + p_0}\right)^{1/3} \quad [6]$$

All bubbles are deleted at the moment they reach the phase boundary between the electrolyte and the air phase, which is indicated by an air phase fraction above 10 pct.

In addition, a two-way coupling between the discrete phase and the continuous phases is applied. Thereby, the continuous phases decelerate the gas bubbles through the drag force. The impact of the gas bubbles on the continuous phase is modeled by applying an additional source term in the Navier–Stokes equations:

$$F_{ex} = \frac{18\mu_C C_D Re_B}{\rho_B d_B^2}(u_B - u_C)\dot{m}_B \Delta t \quad [7]$$

The k-ε turbulence model is used to model turbulences. The CFD simulation is conducted using CFD software ANSYS FLUENT 17.2.

III. RESULTS

For both cells, the electrolyte flow field after 20 seconds is presented by contours and streamlines. By this time, the flow is in a quasi-stationary state. The displayed values are obtained by averaging the node velocities over 0.25 seconds, which correspond to 500 time-steps. In the figures, only the electrolyte phase is shown; the other continuous phases, the air, and, in case of the modern cell, the metal phase, are blanked out. Since the electrolysis cells are axisymmetric, merely the areas between the cell center and the crucible wall are given on a plane through the coordinate origin.

A. *Modern Cell Type*

The fluid velocity distribution within the modern cell with horizontal, liquid cathode is shown in Figure 2(a). After being formed below the anode, the gas bubbles drifts toward the anode edge. Then, the gas bubbles rise, located closely to the anode sidewall, and transfer an impulse on the electrolyte. Due to that, the electrolyte is accelerated to a maximum velocity magnitude of about 0.2 m/s, close to the free surface. As a result, a circulating flow with a large extend is formed closely below the air-electrolyte interface. As can be seen in Figure 2(b), the circulation induces smaller areas of circulating flows that continue cascade like, with decreasing magnitudes, to the edge of the active anode surface.

As shown in Figure 2(b), the main circulating flow, located close to the electrolyte bath surface, is the area with the highest velocity magnitude. This provides a swift dissolution of added Neodymium oxide and, therefore, is desirable for a stable process without

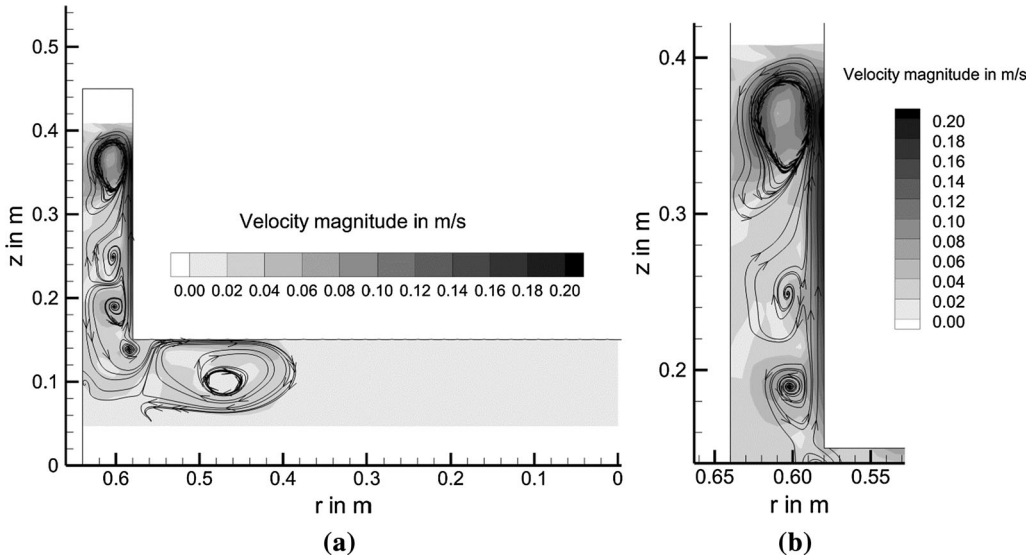

Fig. 2—(*a*) Fluid velocity distribution in a modern cell with liquid bottom cathode and horizontal anode and (*b*) magnification of the area between anode and crucible sidewall.

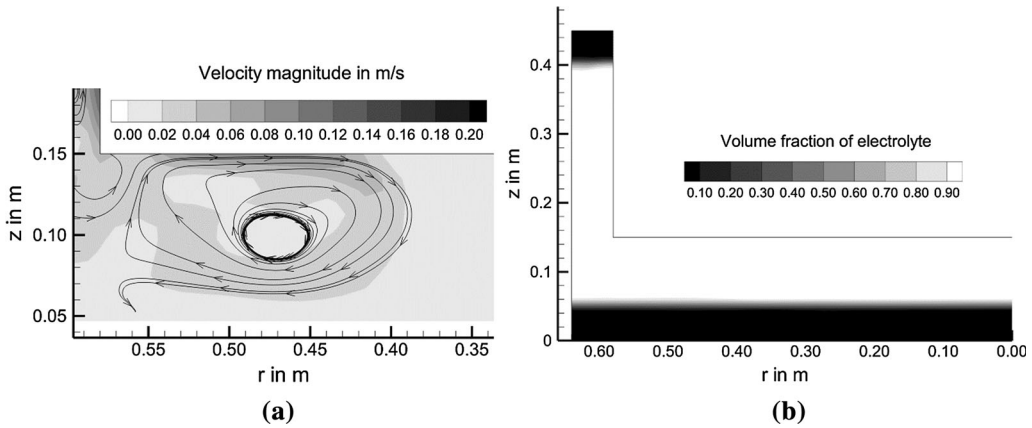

Fig. 3—(*a*) Magnified view of the fluid velocity distribution in the crucial area between anode and liquid cathode and (*b*) distribution of metal phase.

greenhouse gas emission. Another positive aspect is that the upwardly directed flow in deeper circulations counteracts the sedimentation of undissolved oxide particles. By that, an oxide contamination of the molten neodymium metal at the cell bottom is prevented. However, the circulating flow cascade is not extended completely below the anode. Owing to that, there is no convectional mass transfer in this region. This may result in large concentration gradients. Experiments in a laboratory scale are necessary to determine if the diffusional mass transfer or the convectional mass transfer by electromagnetic stirring or natural convection is sufficient to compensate for this disadvantage.

As can be seen in the close-up view in Figure 3(a), the last circulating flow structure is placed below the anode edge. Its extent and velocity magnitude are not sufficient, though, to influence the phase boundary between the electrolyte and the metal phase.

The phase distribution is shown in Figure 3(b). As described previously, the interface between the metal and electrolyte is undisturbed. This should promote a high current efficiency, as product reoxidation is not possible. Moreover, the results reveal a potential to lower the cell voltage by decreasing the electrode distance. Experiments and further numerical studies should be carried out to determine the best trade-off between a low cell voltage and a high current efficiency.

B. *Conventional Cell Type*

The fluid velocity distribution within the conventional cell is shown in Figure 4. Rising gas bubbles induce a circulating flow between the inserted anode and cathode with a maximum velocity of about 0.2 m/s. The circulating flow extends over the entire area between the electrodes, but its center is located close to the anode, below the free surface. As in the modern cell, the circulating flow provides high dissolution rates of added Neodymium oxide. The circulation velocity in the deeper electrolyte region, especially close to the cathode,

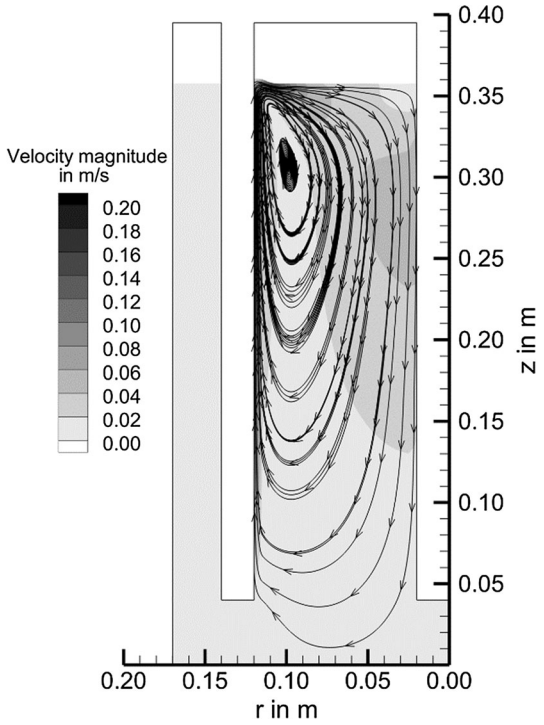

Fig. 4—Fluid velocity distribution in conventional cell with vertical injected cathode.

is low. Therefore, the metal collected in the tungsten crucible at the cell bottom, placed below the cathode, is not affected. However, the buoyancy-driven sedimentation of reduced metal might be disturbed. The electrolyte flow, which is directed away from the cathode in the lower cell region, might transport already reduced neodymium droplets toward the anode. A contact between metal droplets and the anode, or even the off-gas, would cause massive product reoxidation. By this phenomenon, the low current efficiency, observed in the currently operated cells, can be explained. Owing to that, a reduction of the electrode distance would cause a further reduction of the current efficiency, because the risk of product reoxidation would be enhanced. Therefore, the specific energy cannot be decreased in the conventional cell.

An advantage of the currently operated cells is that the average residence time of gas bubbles is very short. After being formed, the bubbles can rise freely, while they have to drift outwardly below the horizontal anode in the novel cell type. Owing to that, the risk of partial anode passivation is much lower. Moreover, there is convectional mass transfer between both electrodes. By that, local concentration gradients should not occur.

C. *Validation*

Since no setup to validate the model experimentally is avialable, the results are compared to literature data. Wang *et al.*[8] studied the velocity distribution in a 10-kA reduction cell with horizontally arranged electrodes by using ANSYS FLUENT. In a two-dimensional computation area, the bubble diameter was estimated as 10 mm and its rising process was modeled by the Euler–Euler model. In their model, a maximum electrolyte velocity magnitude of 0.25 m/s was found. This value is close to the maximum electrolyte velocity of 0.26 m/s found in this work. Moreover, a similar circulating flow structure in the gap between the anode sidewall and crucible was found. In contrast to the results of this work, the flow consists of only one circulating structure, though, which extends over the entire gap area. Moreover, the maximum absolute bubble rising velocity was found to be 1.39 m/s. In this work, the absolute rising velocity was only about 0.5 m/s.

Feng *et al.*[19] studied the flow structure of the continous phase in the gap area by digital particle image velocimetry in a water model of the Hall–Héroult cell. As in this work, a circulating flow with the same circulation direction was found. The circulation extended over the entire gap area, though. This might be explained by the gap width-to-height ratio, which was much higher compared to that of the cell used in the present model.

Wang *et al.*[8] and Ren *et al.*[9] modeled the flow field within the conventional cell. Again, the results are in close agreement with the model presented in this work. Due to the absence of their numerical data, quantitative comparison is not possible, though. In contrast to this work, He found a weaker circular flow between the lower edges of the electrodes, which might be caused by electromagnetic force.

In order to validate the accuracy of the model, once again, the calculated relative bubble velocity is compared to theoretical values obtained from the literature. According to Newton's second law, a body changes neither its direction nor its velocity in the case in which no net force is acting on this body. Assuming that the impact of all forces except the buoyancy force (Eq. [1]) and the drag force (Eq. [3]) is negligible, the terminal rising velocity of a bubble can be obtained by equating both forces. By this, it can be shown that the terminal rising velocity is given by

$$u_B = \sqrt{\frac{4(\rho_C - \rho_B) g d_B}{3 \rho_C C_D}} + u_C \qquad [8]$$

As indicated previously, numerous correlations for the drag coefficient C_D are available. A selection of those is summarized in Table III. The resulting relative velocity is calculated by the drag coefficient and Eq. [8]. For the calculation, the Eötvös number is 2.36 while the Morton number is 5.67×10^{-10}, calculated with the employed fluid properties summarized in Table II. The Reynolds number is obtained iteratively, since it is a function of the relative velocity.

In both models presented in this work, the average relative bubble velocity is found to be 0.22 m/s, which is in excellent agreement with the predicted relative velocities summarized in Table III.

Table III. Drag Coefficient Correlations

References	Drag Correlation	Relative Velocity (m/s)
16	Eq. 4	0.23
20	$C_D = \max\left\{\frac{24}{\mathrm{Re}}\left(1 + 0.1\ \mathrm{Re}^{0.75}\right), \min\left[\frac{2}{3}\sqrt{\mathrm{Eo}}, \frac{8}{3}\right]\right\}$	0.23
21	$C_D = \frac{24}{\mathrm{Re}}\left(1 + 0.15\mathrm{Re}^{0.687}\right)$	0.31
22	$C_D = \max\left\{\max\left[\frac{24}{\mathrm{Re}}, \frac{18.7}{\mathrm{Re}^{0.68}}\right], \min\left[0.0275\mathrm{Mo}\cdot\mathrm{Re}^4, 0.83\mathrm{M}^{0.25}\mathrm{Re}\right]\right\}$	0.35
23	$C_D = f\left(\frac{a}{R_{eq}}\right)^2$	0.25

Table IV. Comparison of Modern and Conventional Cell Design

Parameter	Modern Cell	Conventional Cell
Product reoxidation	low probability	high probability
Electrode distance reduction	possible	impossible
Dissolution rate oxide	high	high
Dwelling time gas bubbles	high	low
Convectional mass transport	between crucible and anode	between anode and cathode
Free surface area	low	high
Dead volume	not existing	existing
Product withdrawal	pump system	ladle

IV. DISCUSSION

In terms of the fluid flow, the novel cell design, which is currently in development, has many advantages over the conventional reduction cell. In Table IV, the most decisive process characteristics of both cells are summarized and evaluated. In the case of the modern cell design, the low probability of product reoxidation promises high current efficiencies. Moreover, there is the opportunity to decrease the electrode distance and, by that, the cell voltage. These process characteristics are preconditions for a low specific energy consumption. The introduced numerical model might be a tool to determine the optimal trade-off between these factors. However, an implementation in industrial scale product lines requires some further investigation. A detailed heat balance analysis is necessary, since the introduced Joule heat is significantly decreased by the design optimization pointed out previously. This might be partly outbalanced by the reduction of the free surface and the absence of dead volume in comparison to the conventional cell type. Moreover, the new cell design makes a higher level of automation essential. Especially, the product withdrawal is far more difficult than in the current process, at which it is usually performed with a simple titanium ladle. A point-feeder system, as known from aluminum electrolysis, and an online oxygen concentration measurement system are necessary to overcome the risk of carbon fluoride emission. A disadvantage of the new cell design associated with that might be that almost no convectional mass transport takes place below the anode, as shown in this work. As already pointed out, further investigations of this matter are necessary to determine the magnitude of this problem.

The validation of both numerical models showed that they are in good agreement with the actual process or, more precisely, with the phenomena taken into account, in the case in which the model assumptions are right. To verify these assumptions, further investigations are necessary. The impact of the assumed bubble size needs to be examined. This might be done by either experimental studies or by further numerical parameter studies. As pointed out previously, the bubble behavior below the anode is greatly simplified, due to the absence of appropriate theoretical models that are able to describe the bubble drift and interaction correctly. Further research concerning this matter would enhance the accuracy of the model. Finally, the electromagnetically induced flow should be modeled as well. Although the impulse is assumed to be small, it acts mainly in the critical zone between the electrodes and, therefore, could influence the phase boundary between the metal and electrolyte.

V. CONCLUSIONS

A CFD simulation was conducted to compute the fluid flow distribution within a modern neodymium reduction cell and a conventional one. To make the results comparable, the anode's current density is equal in both calculations. A validation with literature data indicates that the models are certainly in good agreement with the actual cell. The results suggest the following conclusions:

1. In the modern cell, a circulating flow between the anode's sidewall and the crucible was detected that should promote a high oxide dissolution rate.
2. The induced flow below the anode is weak and does not disturb the phase boundary between the electrolyte and metal. Owing to that, the probability for product reoxidation is low. Moreover, this result reveals the potential to decrease the electrode distance.

3. In contrast to that, the probability for product reoxidation is high within the conventional cell. That might explain the relative low current efficiency in the current process.
4. Within both cell designs, the oxide should be added close to the anode to use the electrolyte upward flow to decrease sludge formation and enhance the dissolution rate of added Neodymium oxide.
5. In the modern cell, there is no convective mass transfer toward the cell's center. Further experimental studies are suggested to clarify whether the diffusive mass transfer is sufficient to avoid the emission of environmental hazardous carbon fluoride off-gas, caused by a low oxygen-ion concentration. This problem is not present in the conventional cell.
6. By further improvement of the modern cell design, the specific energy consumption as well as the risk of carbon fluoride emission can be decreased significantly. By that, the process can become more economical as well as ecological. However, an advanced standard of process automation is necessary to operate this cell type.

REFERENCES

1. C.K. Gupta and N. Krishnamurthy: *Extractive Metallurgy of Rare Earth*, CRC Press, Boca Raton, FL, 2005.
2. S. Pang, S. Yan, Z. Li, D. Chen, L. Xu, and B. Zhao: *Chin. J. Rare Met*., 2011, vol. 35, pp. 440–450 (translated from Chinese by Que Z).
3. K. Liu, J. Chen, and X. Wei: *Chin. J. Nonferrous Met*., 2001, vol. 11, pp. 99–101 (translated from Chinese by Pan Q).
4. H. Vogel, B. Flerus, F. Stoffner, and B. Friedrich: *J. Sustainable Metall.—Special Issue: Rare Earths,* 2016.
5. K. Liu, J. Chen, and X. Wei: *Chin. Rare Earths*, 2001, vol. 22, pp. 30–33 (translated from Chinese by Pan Q).
6. Z. Zhang, X. Liang, J. Ju, and G. Xu: *Chinese Society of Rare Earth—Conf. Proc. 2000,* pp. 207–11 (translated from Chinese by Wang J).
7. D. Chen, S. Yan, Z. Li, S. Pang, L. Xu, and X. Guo: *J. Chin. Rare Earth Soc*., 2011, vol. 29, pp. 769–72 (translated from Chinese by Que Z).
8. J. Wang, Z. Zhang, G. Tu, and W. Wu: *Chin. Rare Earths*, 2012, vol. 33, pp. 64–67 (translated from Chinese by Que Z).
9. Y. Ren, X. Kong, and L. Xie: *J. Rare Earths*, 2004, vol. 22, pp. 252–56.
10. S. Fu: *J. Chin. Rare Earth Soc*., 2007, vol. 25, pp. 71–76 (translated from Chinese by Pan Q).
11. C.W. Hirt and B.D. Nichols: *J. Comput. Phys*., 1981, vol. 39, pp. 201–25.
12. K. Liu, J. Chen, and X. Wei: *Rare. Met. Cem. Carbides*., 2000, vol. 143, p. 7 (translated from Chinese by Pan Q).
13. K. Liu, J. Chen, X. Wei, T. Zheng, L. Xie, and X. Kong: *Chin. Rare Earths*, 2000, vol. 21, pp. 37–39 (translated from Chinese by Pan Q).
14. M. Alam, W. Yang, K. Mohanarangam, G. Brooks, and Y. Morsi: *Metall. Mater. Trans. B*, 2013, vol. 44B, pp. 1155–65.
15. T. Frank, J. Shi, and A.D. Burns: *Validation of Eulerian Multiphase Flow Models for Nuclear Safety Applications*, 3rd Internationl Symposium on Two-Phase Flow Modelling and Experimentation, Pisa, 2004.
16. A. Tomiyama, I. Kataoka, I. Zun, and T. Sakaguchi: *JSME Int. J. Ser. B Fluids Thermal. Eng*., 1998, vol. 41, pp. 472–79.
17. A.W.G. de Vries, A. Biesheuvel, and L. van Wijngaarden: *Int. J. Multiphase Flow*, 2002, vol. 28, pp. 1823–35.
18. C. Brücker: *Phys. Fluids*, 1999, vol. 11, pp. 1781–96.
19. M. Yuqing Feng, P. Schwarz, W. Yang, and M. Cooksey: *Metall. Mater. Trans. B*, 2015, vol. 46B, pp. 1959–81.
20. M. Ishii and N. Zuber: *AIChE J*., 1979, vol. 25, pp. 843–55.
21. L. Schiller and A.Z. Naumann: *Ver. Deut. Ing*., 1933, vol. 77, pp. 318–20.
22. F. Peebles and H. Garber: *Chem. Eng. Progr*., 1953, vol. 49, pp. 88–97.
23. G. Bozzano and M. Dente: *Comput. Chem. Eng*., 2001, vol. 25, pp. 571–76.